SAN098-2319J

VALIDATION OF ELECTRICAL-IMPEDANCE TOMOGRAPHY FOR MEASUREMENTS OF MATERIAL DISTRIBUTION IN TWO-PHASE FLOWS

D. L. George and S. L. Ceccio

Department of Mechanical Engineering and Applied Mechanics

University of Michigan

Ann Arbor, Michigan 48109-2121 USA

J. R. Torczynski, K. A. Shollenberger, and T. J. O'Hern

Engineering Sciences Center

Sandia National Laboratories

Albuquerque, New Mexico 87185-0834 USA

Submitted to the *International Journal of Multiphase Flow*

Abstract --- A series of studies is presented in which an electrical-impedance tomography (EIT) system is validated for two-phase flow measurements. The EIT system, developed at Sandia National Laboratories, is described along with the computer algorithm used for reconstructing phase volume fraction profiles. The algorithm is first tested using numerical data and experimental phantom

DISCLAIMER

measurements, with good results. The EIT system is then applied to solid-liquid and gas-liquid flows, and results are compared to an established gamma-densitometry tomography (GDT) system. In the solid-liquid flows, the average solid volume fractions measured by EIT are in good agreement with nominal values; in the gas-liquid flows, average gas volume fractions and radial gas volume fraction profiles from GDT and EIT are also in good agreement.

Key Words: electrical-impedance tomography, bubble column, gas volume fraction, multiphase flow

1. INTRODUCTION

The spatial distribution of materials in multiphase flows is important to many chemical and industrial processes. For example, in indirect coal liquefaction, where a reactive gas is bubbled through a catalyst-laden slurry, a spatially nonuniform gas distribution within the reactor can reduce process efficiency by inducing large-scale, buoyancy-driven recirculating flows (Jackson *et al.,* 1996). Techniques that measure the distribution of each phase in multiphase flows have the potential to improve the control of such processes. They also can be useful for validating computational models of multiphase flows (Plaskowski *et al.,* 1995; Torczynski *et al.,* 1997).

A dilemma encountered in multiphase flow measurements is that probes or instruments should be placed outside the flow domain so as not to disturb the flow itself; yet phase distributions cannot easily be measured from the boundary. Tomography offers a possible solution to this dilemma, and many different tomographic methods have been applied to the measurement of multiphase flows. Examples of these methods include gamma-densitometry tomography (GDT), electrical-impedance tomography

(EIT), magnetic resonance imaging (MRI), acoustic tomography, and positron emission tomography (PET). Several of these methods have been derived from devices for medical applications.

In this paper GDT and EIT are applied to the task of providing spatially resolved information on dispersed multiphase flows. GDT and other radiation-based tomographic methods are relatively mature and can accurately measure spatial phase distributions (Hewitt, 1978; Shollenberger *et al.*, 1997a). Their main disadvantage is the long data collection times required that usually are longer than the time scales of time-dependent multiphase flows. EIT can acquire information much more quickly than GDT, but several issues with EIT have yet to be resolved, including its usefulness for multiphase flows, its spatial resolution, and its ability to make accurate quantitative measurements (Webster, 1990; Jones *et al.*, 1993; Plaskowski *et al.*, 1995; Ceccio and George, 1996). While capacitance sensors have been used to visualize gas-liquid slug flow (Huang *et al.*, 1989) and flows in trickle-bed reactors (Reinecke and Mewes, 1997), the EIT technique must still be validated for quantitative phase volume fraction measurements.

This paper documents a series of studies in which an EIT system developed at Sandia (O'Hern *et al.*, 1995; Torczynski *et al.*, 1996a) and an established GDT technique were used to quantify properties of two-phase flows. Since the Sandia GDT system has already been successfully applied to multiphase flows (Adkins *et al.*, 1996; Torczynski *et al.*, 1996b; Shollenberger *et al.*, 1997a), it was used to assess the accuracy of the EIT system. The paper begins with a brief introduction to EIT theory and a description of the Sandia tomographic reconstruction method and EIT system. Numerical and experimental validation tests of the reconstruction algorithm are then presented. The final section of this paper describes the experimental conditions of the two-phase flow tests and compares results from EIT and GDT. Both solid-liquid flows and gas-liquid flows are examined.

2. ELECTRICAL-IMPEDANCE TOMOGRAPHY SYSTEM

2.1 *EIT theory*

In electrical-impedance tomography, a number of electrodes are mounted to the surface of a domain of interest, **D**. As a prescribed current is injected into the domain at one electrode and withdrawn at another electrode, all electrode voltages are measured relative to ground (Figure 1). These measurements at the domain boundary are then used to reconstruct the impedance distribution within the domain and infer the phase distribution.

In practice alternating current (AC) is used to avoid polarization effects on the electrodes. For AC electrical conduction with field frequencies on the order of tens of megahertz or lower, the electric potential V within the domain **D** is related to the complex electrical conductivity γ of the domain by

$$\nabla \cdot \gamma \nabla V = 0 . \qquad [1]$$

Equation 1 assumes no charge sources or sinks are present in **D**. The boundary conditions on **D** are given by

$$\mathbf{n} \cdot \gamma \nabla V + q'' = 0 , \qquad [2]$$

where **n** is the unit normal vector outward from the domain boundary, and q'' is the charge flux on the boundary. Multiple measurements of q'' and V at the boundary are used to iteratively reconstruct the conductivity distribution within **D** that yields the measured boundary conditions.

In practice, current injections and voltage measurements are performed at a finite number of boundary locations — *i.e.*, electrodes — and the limited resolution of the reconstructed conductivity field will be strongly related to the number and locations of the electrodes. If N electrodes are used, the domain can be modeled as an N-port impedance network, where a current source and current sink are placed on two of the ports, and the resulting voltage distribution around the network is measured at the remaining ports. One port, often the current sink, is referenced to ground. The total number of linearly independent voltage measurements R_N in the network is given by

$$R_N = \frac{N(N-1)}{2}. \qquad [3]$$

R_N is also the number of independent impedance elements that can be determined from these voltage projections and used to model the domain.

Several simplifications are generally employed in EIT that make it possible to reconstruct the domain using discrete finite-element methods. One common assumption is that current travels only in a two-dimensional domain. While three-dimensional current flow has been used for some elementary cases, including the vertical bubble-column flows in this work, full three-dimensional EIT reconstruction would require computational effort and resources that are impractical at this time. Other simplifications include the representation of conductivity by a piecewise constant function and mathematical models to

represent the voltage in the domain. It is also assumed in EIT that the impedance distribution within the domain does not change significantly over time while voltage projections are acquired. As a result, EIT systems must acquire projections rapidly, on time scales shorter than the characteristic time scales of multiphase flows.

To reconstruct the image of the domain, a "candidate" impedance distribution is first constructed. A set of voltage projections is then computed from the distribution and compared to voltages measured on the boundary during current injection. Next, the candidate impedance distribution is modified based on the difference between computed and measured voltages, and a new set of voltage projections is computed. This process continues until some minimum error criterion is satisfied. EIT reconstruction is an ill-conditioned problem; as a result, the reconstructed impedance "solution" will be sensitive to noise in the projections and may not satisfy requirements of existence or continuous dependence on the problem data. The ill-conditioning and the sensitivity to noise increase as the number of electrodes and the spatial resolution of the solution increase. *A priori* knowledge of the impedance distribution may be used to aid in reconstruction, but in most multiphase flows, such information is not readily available.

More information on EIT theory and the development of EIT systems for the study of multiphase flows may be found in Dickin *et al.* (1993); Jones *et al.* (1992, 1993, 1994); and Ceccio and George (1996).

2.2 *Finite-element method for reconstruction of conductivity distributions*

The reconstruction algorithm used with the Sandia EIT system has been described in detail by Torczynski *et al.* (1996a, 1997) and is based on the YWT method described by Yorkey *et al.* (1987). This section summarizes the method.

In the algorithm, the medium is treated as purely resistive, with no capacitive contribution, which is reasonable for the multiphase flows considered here. The medium is surrounded by an insulating boundary through which current is injected or withdrawn at discrete electrodes. A finite-element method (FEM) representation is generated for the voltage equation, identical in form to the steady-state heat-conduction equation. The electrical conductivity is represented as a function of position and one or more conductivity parameters. For the boundary conditions, current flow is specified at the electrodes such that the net current into and out of the domain is zero.

The finite-element equations generated from Eq. 1 are solved to find both the predicted voltages at the electrodes and the derivatives of the electrode voltages with respect to the conductivity parameters. Since no voltages are prescribed in the computational boundary conditions, the computed voltage solution of Eq. 1 is unique only to within an arbitrary additive constant. Subsequently, the conductivity parameters are adjusted by a Newton-Raphson algorithm to minimize the least-squares difference between the computed and experimental electrode voltages at the non-current-bearing electrodes. The value of the additive constant is determined during the least-squares minimization process.

Separate computer codes have been written to implement this algorithm in two and three dimensions. The two-dimensional code FEMEIT models arbitrary domains and represents electrodes by mesh nodes, essentially mathematical points. FEMEIT generates and solves the FEM equations using global conductivity functions from a subroutine library and applies the Newton-Raphson algorithm to determine the final conductivity parameters. Conductivity functions in the library include a constant conductivity, a circular insulating region at an arbitrary position, and various analytical conductivity distributions. As an example, the following formula is used for the spatial variation of conductivity $\gamma(x,y)$ in the case of a circular insulator (Torczynski *et al.*, 1996a):

$$\gamma = c_1\left\{1+\frac{p_1}{2}\left[\tanh\left(\frac{w-c_2}{p_2}\right)-\tanh\left(\frac{w+c_2}{p_2}\right)\right]\right\}, \qquad [4]$$

where

$$w^2 = (x-c_3)^2+(y-c_4)^2. \qquad [5]$$

This function represents a circular region of radius c_2 centered at (c_3, c_4) with a boundary thickness proportional to $2p_2$. Well inside the circular region, the conductivity is approximately $c_1(1 - p_1)$ and well outside, the conductivity is approximately c_1. With proper choices of the parameters p_1 and p_2, this function represents an insulating cylinder of varying position and radius.

For three-dimensional computations, the FEM equations are generated and solved separately using the finite-element code FIDAP (Fluid Dynamics International, 1995). Using FEM solutions from FIDAP, library files have been created that map fundamental electrode voltages in parameter space, assuming only radial variations in the conductivity field. The library files are used with the codes EITCON and EITAXI, which use cubic-spline interpolation and a Newton-Raphson algorithm to determine the final conductivity parameters. EITCON solves for the gas volume fraction ε_G directly, assuming a uniform conductivity across the domain, whereas EITAXI solves for coefficients of other conductivity distributions, such as a second-order polynomial or a cylindrical insulating inclusion centered in the domain. As an example, the parabolic radial profile reconstructed by EITAXI takes the form

$$\frac{\gamma(r)}{\gamma_L} = \frac{1 + c[2(r/R)^2 - 1]}{b}, \qquad [6]$$

where γ_L is the liquid conductivity, b is a scale parameter, c is the parabolic conductivity shape parameter, r is the radial coordinate, and R is the radius of the circular domain, *e.g.*, the bubble column.

As part of the normal reconstruction process, FIDAP generates a set of nondimensional, fundamental voltage solutions, $\{V_0 \ldots V_{N/2}\}$, for the parameter libraries used by EITCON and EITAXI to evaluate experimental data. The supplementary computer code EITFUN was written to compute fundamental voltage solutions from axisymmetric experimental data sets, the reverse of the usual process. Comparisons of the computational and experimental fundamental solutions for no-flow conditions allowed an evaluation of different electrode geometries; the results of this comparison are described in section 2.4.

2.3 *Determination of volume fraction distributions from conductivity distributions*

With the converged parameters from FEMEIT or EITAXI the conductivity distribution can be constructed, and information such as the domain-averaged gas volume fraction $\bar{\varepsilon}_G$ can be found from a constitutive model. The Maxwell-Hewitt relation (Maxwell, 1881; Hewitt, 1978) is used in this work to relate the local mixture conductivity $\gamma(r)$ and the liquid conductivity γ_L to the local gas volume fraction $\varepsilon_G(r)$:

$$\varepsilon_G^{3D}(r) = \frac{1 - [\gamma(r)/\gamma_L]}{1 + \frac{1}{2}[\gamma(r)/\gamma_L]}. \qquad [7]$$

The expression above assumes three-dimensional inclusions of an insulating phase in a conducting phase, such as gas bubbles or dielectric solid particles dispersed in water. Applying the same derivation to a two-dimensional case (*e.g.*, cylindrical inclusions in a cylindrical domain) yields a similar expression:

$$\varepsilon_G^{2D}(r) = \frac{1-[\gamma(r)/\gamma_L]}{1+[\gamma(r)/\gamma_L]}. \qquad [8]$$

To determine the domain-averaged gas volume fraction $\bar{\varepsilon}_G$, the profiles can be analytically integrated over the domain. If an insulating solid phase is present instead of a gas, the same expressions will yield $\varepsilon_S(r)$.

The values of γ_L used to obtain phase volume fractions in all experiments were determined with the EIT system itself, using measurements of the domain with only liquid present. A good measurement of liquid conductivity is crucial for obtaining quantitative data and requires careful control of test conditions, since conductivity can vary significantly with temperature and the presence of contaminants in the liquid.

2.4 *Sandia EIT system*

A block diagram of the EIT system (Torczynski *et al.*, 1997; George *et al.*, 1998) is shown in Figure 2. The system consists of an electrode array; a signal generator; a voltage-controlled current source; multiplexers connecting the electrode array to the current source, ground, and measurement electronics; an instrumentation amplifier and phase-sensitive demodulators; and a data acquisition card. The data acquisition card contains an analog-to-digital converter that measures the demodulated DC signals and a

digital controller that can be used to select electrodes for current injection, ground, and measurement. The card also acts as an interface to a PC that operates the entire system.

During operation, the EIT system injects a controlled current through one electrode, "sinks" a second electrode to ground, and measures voltages at all electrodes relative to ground. For completeness, a "projection set" consists of measurements at all N electrodes for each injection and ground combination, for a total of $N^2(N\text{-}1)/2$ voltage measurements. The domain is excited with a 50-kHz AC electric field, a frequency at which the resistive component of impedance dominates for air-water and polystyrene-water flows (Ceccio and George, 1996). The voltage signals from each electrode pass through an amplifier to a phase-sensitive demodulator that separates the signal into two components: one in phase with the EIT carrier signal, the other out of phase with the carrier by 90°. These components are DC filtered to yield the carrier and quadrature components, respectively, of the measured voltage.

Commands issued to the multiplexers determine which electrodes are selected for current injection, grounding, and voltage measurement. Originally the software issued these commands through the data acquisition card's digital controller. Later, integrated circuit (IC) counters were added to the EIT hardware to select injection, ground, and measurement electrodes in sequence. For sixteen electrodes, the acquisition time for each voltage projection set was reduced from 2.7 seconds with the software command option to less than 0.75 seconds with IC counters. For this reason, the software-controlled option is called "slow mode," while the IC-controlled option is referred to as "fast mode" (see, for example, Table 3). Validation tests were conducted using both fast and slow modes to examine the impact of the faster acquisition time on reconstruction accuracy. The results of this comparison are described in the next section.

The electrode array discussed in this paper was fabricated for use both in validation tests and in experiments conducted in a transparent bubble column. Sixteen electrodes were fashioned from stainless steel strips 0.64 cm wide, 7.62 cm high, and 76 μm thick. These were mounted at equal azimuthal intervals in a Lucite cylinder with an inner diameter of 19.05 cm, a wall thickness of 0.64 cm, and a height of 12.7 cm (Figure 3). Other electrode arrays with square and circular electrodes 1.27 cm across were used during some experiments in order to evaluate the merits of different electrode geometries. The evaluation used measurements of baseline liquid conductivities taken with each electrode ring before gas-liquid tests. Fundamental solutions were derived from these no-flow data with EITFUN and compared to calculated solutions from FIDAP for a uniform conductivity field in three dimensions. The fundamental voltages from the square and circular electrode data were in poor agreement with calculated values. At all non-current-bearing electrodes the experimental voltages were similar. Besides implying a potential for significant disagreement between actual and calculated conductivity profiles, this similarity indicated that under multiphase flow conditions, the electrodes would have poor sensitivity to variations in the conductivity profile. In contrast, the fundamental voltage solutions from strip electrode data were in excellent agreement with the computational values at the non-current-bearing electrodes 0 through 7 (Table 1). Although the voltages at the current-bearing electrode (V_8) differ somewhat, the reconstruction algorithm does not use this quantity (Torczynski *et al.*, 1996a and 1997). The voltages at non-current-bearing electrodes varied significantly from one electrode to the next, implying a higher sensitivity to changes in the domain conductivity profile. As seen in Table 1, multiplying the experimental values by 1.007 brings them into agreement with computed voltages to almost three significant figures. A difference of 0.7% between computational and experimental voltages is reasonable, since experimental error in injected current and liquid conductivity

are about 0.5% and computational accuracy is similar. Based on these results, strip electrode data were used exclusively to reconstruct radial profiles of the multiphase flows.

3. VALIDATION OF RECONSTRUCTION ALGORITHM

3.1 *Numerical validation of conductivity reconstruction algorithm*

Several calculations were performed to validate the reconstruction algorithm. The first test involved an analytical result for the two-dimensional voltage distribution $V(x,y)$ in a circular domain of constant conductivity γ. The boundary conditions were defined by a current per unit length, J, injected at the boundary point (x_o, y_o) and withdrawn at the boundary point $(x_o,- y_o)$; this yielded the analytical result

$$V(x, y) = (J / 2\pi\gamma) \ln\left[\frac{(y_o + y)^2 + (x_o - x)^2}{(y_o - y)^2 + (x_o - x)^2}\right]. \qquad [9]$$

The uniform domain was bounded by 16 electrodes located at equal intervals of 22.5° around the perimeter. The radius of the circular domain, the current per unit length J, and the conductivity γwere all set to unity. By rotating the coordinates of the analytical results from selected injection and withdrawal combinations, the boundary voltages for all possible injection and withdrawal pairs were determined from the analytical solutions. These analytical voltages were input to FEMEIT, along with mesh information, to find the effect of mesh size on reconstruction accuracy. The conductivity function was chosen to be a single unknown constant throughout the domain. Table 2 shows the dependence of the constant conductivity determined by FEMEIT for five meshes of appreciably different nodal density;

an ideal result would be a calculated conductivity of unity. In all cases the calculated result is close to unity, and is converging to unity with increasing nodal density (Torczynski *et al.*, 1996a).

In the second set of validation calculations, the finite-element code FIDAP was used to compute the boundary voltages corresponding to the synthetic spatial conductivity distribution shown in Figure 4. This distribution mimics a bubble-column flow with an excess of bubbles in the upper right quadrant. The electrode geometry was identical to that used in the first problem, but a highly refined mesh was used to guarantee that the FIDAP solution would be mesh-independent. The computed voltages from FIDAP were input to FEMEIT to test its ability to reproduce the original conductivity distribution. Figure 5 shows the mesh used for this simulation (identical to mesh E of Table 2) and the reconstructed conductivity field produced by the EIT algorithm, where FIDAP has been used to post-process the FEMEIT results. Agreement is again seen to be good.

3.2 *Experimental validation of reconstructed conductivity profiles*

The next step in validating the algorithm involved experimental data. Validation experiments were performed by capping the bottom of the cylinder containing the electrode array (Figure 3) to form a static testbed, filling the testbed with a saltwater solution of known conductivity, and placing smaller Lucite cylinders of known radii in the testbed to act as insulating inclusions. EIT voltage measurements were then taken of the domain and used to reconstruct the location and position of the insulating "phantom."

To limit the test domain in the vertical direction, the free surface of the liquid and the bottom Lexan end cap were aligned with the top and bottom ends of the strip electrodes, respectively. This eliminated axial electric field variations and enforced two-dimensionality. Cylinders of different diameters were placed both eccentrically and concentrically with the testbed axis to mimic different distributions of gas

in a bubble column. Data were acquired using both the PC software ("slow mode") and IC counters ("fast mode") to select electrode combinations.

Eqs. 4 and 5 were employed as the spatial conductivity function in the FEMEIT reconstructions. Table 3 presents, for each test case, the actual diameter d of the test object and the offset distance z of the object center from the testbed central axis, both normalized by the domain radius R. The table also presents the computed diameter $d = 2c_2$ and offset distance $z = \sqrt{c_3^2 + c_4^2}$, determined from the EIT data and normalized in the same manner. A domain-averaged volume fraction, $\bar{\varepsilon} = (d/2R)^2$, was also computed from the actual and reconstructed object dimensions. For all cases the conducting medium was deionized water with sodium chloride solution added to yield a conductivity of $\gamma = 420 \pm 5$ μS/cm. Figure 6 shows the reconstructed conductivity distributions for two of the four test cases; red indicates regions of high conductivity, and blue indicates low conductivity.

The reconstructions are in good agreement with actual conditions, reproducing the volume fraction to within 0.005 in $\bar{\varepsilon}$ and the distance of the inclusion from the central axis to within 3%. For the smaller inclusions the diameter of the object (and hence the average volume fraction) was always slightly overpredicted; furthermore, a small object was produced by the reconstruction algorithm when none was present. The source of this error is believed to be differences between the measured and reconstructed voltages along the domain boundary. An example of these differences can be found by comparing the progression of fundamental voltages $\{V_1 \ldots V_7\}$ in Table 1. While the computed voltages match the corrected experimental data to within 1% at each electrode, changes in the sign and magnitude of the discrepancy indicate slightly different "shapes" of the computed and experimental voltage profiles along the boundary. This would produce slight differences between the actual and reconstructed conductivity profiles.

In the case of the largest test object, the volume fraction was underpredicted. Electrical-impedance methods are known to become less effective as the insulating portion of the domain increases and the electric field becomes less uniform (Ceccio and George, 1996). Tests with the largest object are believed to fall into the region of decreased sensitivity of the EIT system.

3.3 *Validation of Maxwell-Hewitt relations*

To investigate the assumptions used in multiphase flow experiments to compute volume fractions from measured conductivity data, the accuracy of the Maxwell-Hewitt relations (Eqs. 7 and 8) was assessed. FIDAP was used to perform exact numerical simulations of the voltage field in various periodic geometries. Two-dimensional square lattices of insulating squares, circles, and diamonds (squares rotated by 45°), and three-dimensional simple-cubic lattices of cubes and spheres were modeled in a "liquid" domain. The geometry was defined such that without an inclusion, unity current would pass through the domain; with an inclusion present the current was reduced from unity by the ratio of the effective conductivity $\bar{\gamma}$ to the actual liquid conductivity γ_L (per Ohm's Law).

Figure 7 compares these effective conductivity ratios with values predicted by the two-dimensional and three-dimensional Maxwell-Hewitt relations. The symbols represent FIDAP results, which are the exact solutions for converting conductivity measurements to insulating volume fractions. The dashed lines are values predicted by Eqs. 7 and 8. Bounding values, determined by cases where current travels through a single layer of liquid and a single layer of gas arranged in "series" or "parallel," are also plotted as solid lines (the bounding case of phases in series lies on the lower horizontal axis). It can be seen that, except for two-dimensional diamonds, using the Maxwell-Hewitt relations for insulating objects of these shapes will cause the insulating phase volume fraction to be only slightly overestimated.

The results for circles and spheres closely follow the Maxwell-Hewitt relations until the inclusions touch. It is concluded that these relations are of uniformly good accuracy so long as inclusions are not highly distorted and can "fill space without overlapping." A recursive application of the three-dimensional Maxwell-Hewitt relation for a bimodal bubble-size distribution, such as might be found in churn-turbulent flow, showed that the insulating phase volume fraction would be slightly overpredicted if computed under the assumption of a monodisperse size distribution instead.

4. EXPERIMENTAL MEASUREMENTS OF TWO-PHASE FLOWS

The EIT system was applied to *in situ* measurement of dispersed two-phase flows. Both solid-liquid and gas-liquid flows were studied to determine the ability of EIT to measure volume-averaged phase fractions. In the solid-liquid tests, the mixture properties varied smoothly over scales much larger than the size of the dispersed solid phase but much smaller than the size of the test vessel. In the gas-liquid bubbly flows, the scale of the dispersed phase (air bubbles) was larger than in the solid-liquid mixture but still small compared to the scale of the apparatus.

Liquid conductivity was controlled by adding sodium nitrate to deionized water, ensuring that resistive effects would dominate over capacitive effects in EIT measurements. For resistance to dominate, the following constraint on the liquid conductivity must be satisfied:

$$\gamma_L >> 2\pi f \tilde{\varepsilon} \varepsilon_0 , \qquad [10]$$

where f is the AC frequency, $\tilde{\varepsilon}$ is the normalized permittivity (or dielectric constant) of the liquid medium, and ε_0 is the permittivity of a vacuum. For f = 50 kHz in water, this constraint is satisfied if γ_L >> 2 μS/cm; experimental conductivities were chosen to be at least one hundred times higher than this value.

The governing equation for the computational domain, Eq. 1, assumes no charge sources or sinks are present in the domain. For multiphase experiments, this assumption requires that no grounded conductors (except for the withdrawal electrode) may be in contact with the conducting medium anywhere within 10 column diameters of the electrode ring. To enforce this requirement, only electrically isolated instruments (cartridge heaters and thermocouples) were allowed at the flow boundaries, and mechanical devices within the flows were electrically isolated or given non-conducting coatings.

4.1 *Sandia GDT system*

For validation of the EIT system *in situ*, phase distribution measurements were also made with a gamma-densitometry tomography (GDT) system developed at Sandia for studies of industrial-scale multiphase flows (Torczynski *et al*, 1996b; Shollenberger *et al.*, 1997a). The GDT system, shown in Figure 8, employs a 5-curie ^{137}Cs gamma source, a sodium-iodide scintillation detector system, a computer-controlled traverse to position the source and detector, and data acquisition hardware and software. Measurements of gamma-ray attenuation are taken along many parallel beam paths and translated into a gamma attenuation coefficient, μ, averaged along each path. Attenuation by the testbed walls is subtracted from the raw data; then a time-averaged, normalized radial attenuation distribution is reconstructed using the Abel transform (*cf.* Vest, 1985) and the assumption of an axisymmetric phase

distribution. The axisymmetric assumption is valid over the long acquisition time scales of GDT, which range from fifteen to thirty minutes for gas-liquid flows. Attenuation profiles from the GDT system are routinely checked to verify that the axisymmetry assumption is valid.

For gas-liquid flows, the attenuation information may be converted to a gas volume fraction profile, ε_G, through the formula

$$\varepsilon_G^{GDT}(r,R) = \frac{\mu_L - \mu(r,R)}{\mu_L - \mu_G}, \qquad [11]$$

where r is the radial coordinate, R is the radius of the circular domain, and the attenuation coefficients of the liquid and gas (μ_L and μ_G, respectively) have been previously measured or are known *a priori*. Since the attenuation distribution is axisymmetric, both the attenuation and phase distributions are modeled as polynomials with only even powers of r. By substituting an analytically averaged gamma attenuation coefficient, $\overline{\mu}$, for $\mu(r,R)$ in the equation, a domain-averaged phase volume fraction may also be obtained. In addition, the GDT system may be used for measurements of solid-liquid flows if the attenuation coefficients of the solid and liquid are significantly different.

4.2 *Solid-liquid experiments*

The first EIT validation experiment involved a closed container of conducting liquid with a flow of insulating solid particles. This solid-liquid flow was chosen for two reasons. First, the amount of solid introduced into the container can be carefully controlled, providing a good check of the tomography

results. Second, unlike gas bubbles, solid particles can be small, uniform spheres that do not change shape during the experiment, so long as conditions are not harsh enough to fracture the particles.

Schematic diagrams of the experimental setup are shown in Figure 9. The testbed consisted of the strip-electrode cylinder stacked between two Lexan cylinders of the same inner diameter and wall thickness. This testbed, 81.3 cm in height, was capped at the bottom and the top, and a Sargent-Welch mixer was inserted into the cylinder through a small hole in the center of the top cap. The mixer was used to generate a relatively uniform solids distribution inside the cylinder; to prevent settling of the solids, the mixer impeller was positioned 1.27 cm above the lower cap. Since the mixer's shaft was not long enough to reach out of the cylinder, an insulating Lexan extender joined the end of the shaft to a second shaft connected to the Sargent-Welch mixer motor mounted above the testbed. An "overflow" volume was placed above the top cap to eliminate free-surface effects — *e.g.*, a vortical "funnel" — in the cylinder interior during mixing.

Although the mixer shaft was small compared to the test cylinder (the ratio of their diameters was 0.042), the presence of the shaft posed problems for EIT. Placing an electrical conductor in the center of the testbed had the potential to significantly distort the electric field lines, so the steel shaft and impeller were coated with a layer of insulating paint to mitigate this effect. Earlier EIT measurements with and without the mixer shaft in place, with no particles present, verified that the insulated shaft had only a small effect on EIT behavior (Shollenberger *et al.*, 1997b).

As discussed above, the liquid phase was deionized water with a small amount of saturated sodium nitrate solution added for conductivity control. For the solid phase, polystyrene spheres were used with a density of 1.04 g/cm^3 and a range of diameters from 200 to 500 μm. Polystyrene is an insulator with respect to water, so EIT is able to discriminate between the solid and liquid phases. EIT measurements

were compared to the nominal cylinder-averaged solid volume fraction $\bar{\varepsilon}_S^{NOM}$, computed from the density and total mass of polystyrene added to the testbed. GDT is not useful in this case because the attenuation coefficients of polystyrene and water are too similar for the phases to be distinguished [μ_L = 0.0856 cm^{-1}, μ_S = 0.0866 cm^{-1} (Thoraeus, 1965)]. Insulating solids that have attenuation coefficients significantly different from water typically have a much higher specific gravity and are difficult to loft uniformly (Shollenberger *et al.*, 1997b).

For each value of $\bar{\varepsilon}_S^{NOM}$, the required mass of spheres was introduced into the testbed, and liquid was added to occupy the remaining volume. A mixer speed of 420 rpm was applied for 30 minutes to all solid loadings so that a roughly uniform distribution of particles was observed visually within the liquid during measurements. EIT voltage measurements were repeated over the thirty-minute stirring period to verify that a steady-state distribution had been attained. Mixing was then terminated, and the spheres were allowed to settle to the bottom of the cylinder. Following this settling period, EIT was applied again. The second EIT measurement was necessary for calibration purposes; despite attempts to wash and rinse the polystyrene particles before the experiments, soluble contaminants were introduced with the particles that altered the conductivity of the water. The magnitude of this effect on the water conductivity was comparable to that of the suspended solid particles during mixing.

Analysis of the data with EITAXI demonstrated that the radial solids profiles were relatively uniform: radial variations in the local solids density ε_S were less than 0.01 across the domain, and were on a scale much larger than the diameters of the particles themselves. The radial data were analytically integrated to obtain cross-sectionally-averaged solid volume fractions, which are plotted in Figure 10. The solid volume fractions determined by EIT are seen to be in close agreement in all cases with the nominal values computed from the mass of added particles, validating the method for solid-liquid

measurements. The difference between measured and nominal values becomes more negative with increasing solid volume fraction, approaching $\bar{\varepsilon}_S^{EIT} - \bar{\varepsilon}_S^{NOM} = -0.003$ when $\bar{\varepsilon}_S^{NOM} = 0.050$. It is possible that the ability of the mixer to produce a uniform axial distribution dropped with increased solid loadings, so that the solid volume fraction was slightly less than the nominal value near the top of the cylinder and slightly larger at the bottom. Another explanation for this trend is that a small amount of solids was observed escaping through the hole in the top cap during stirring. These solids passed into the overflow volume, reducing the actual amount of solids in the measurement volume. The fraction of total solids lost to the overflow volume may have increased with nominal loading, causing the observed trend.

4.3 *Gas-liquid experiments*

Gas-liquid tests of the EIT system were conducted in a transparent bubble column assembled at Sandia as a testbed for optical, electrical, and radiation-based multiphase flow diagnostics (Torczynski et al., 1997). The Lexan column, shown in Figures 8 and 11, has an inner diameter D of 19.05 cm; a wall thickness of 0.64 cm; and is built from interchangeable sections so that different diagnostic tools can be placed in the column. In this study, the EIT electrode section was placed near the center of the column. The 16 strip electrodes were centered on a plane $L = 97.16$ cm above the base, at a height-to-diameter ratio of $L/D = 5.1$. The column was filled with water to a depth H_o of 1.45 m, for a height-to-diameter ratio of 7.6; this depth placed the region of EIT sensitivity completely under water. Air can be introduced at volumetric flow rates up to 600 L/min through one of several interchangeable spargers at the base of the column. The spargers are electrically isolated to prevent interference with the EIT system. The column operates at ambient conditions, but the water is subject to evaporative cooling as air

is bubbled through; the liquid temperature was held constant by active heating to within ±0.2°C during experiments, which limited variations in conductivity with temperature to ±0.3%.

The goal for the gas-liquid tests was to validate EIT against GDT in a flow with variations on a larger scale than the solid-liquid flows. A comparison of the two methods was made in churn-turbulent flows in a vertical column; such flows normally have time-averaged volume fraction profiles that are approximately parabolic and can therefore be reconstructed by both the GDT and EIT algorithms. The sparger used to produce churn-turbulent flows is shown in Figure 12. This sparger is a hollow stainless steel toroid with a 10.16-cm centerline diameter, an inner tube diameter of 0.95 cm, and ten holes of diameter 0.16 cm facing downward.

Churn-turbulent experiments were performed using five flow rates: 25, 50, 75, 100 and 150 L/min. The corresponding superficial gas velocities range from 1.5 to 8.8 cm/s. Figure 13 shows the flow conditions in the column for the minimum and maximum flow rates. At the lowest flow condition, a range of bubble sizes was evident, as was a central helical bubble stream. At rates of 75 L/min and above, the flow was completely opaque and turbulent to the naked eye. For each flow condition, 25 full EIT projection sets taken over a period of less than 20 seconds were averaged to obtain the voltage data for reconstructions. Multiple data sets were averaged to enable direct comparison with GDT results, which are inherently time-averaged, and to allow use of axisymmetric reconstruction algorithms. The conductivity of the water used in the gas-liquid experiments was 285±5 μS/cm. GDT measurements were taken in a plane 81.0 cm above the column floor (L/D = 4.25), a location chosen to avoid obstruction by the electrodes.

In the EIT reconstructions, the three-dimensional algorithm was used with the assumption of the parabolic profile given by Eq. 6. Similarly, chord-averaged attenuation coefficients computed from

GDT data were fit to a second- or fourth-order polynomial before the Abel transform was taken. The choice of polynomial for each fit was made based upon the least-squares error between the fit and the attenuation data. Figure 14 shows the gas volume profiles measured by both methods for all volumetric flow rates. The EIT profile tends to lie slightly above the GDT profile at each flow rate, which is consistent with the earlier tendency of EIT phantom reconstructions to overpredict actual conditions. The GDT and EIT gas volume fractions are in excellent agreement, however, falling within 0.01 of each other at all radial positions. Since the change in the local volume fraction across the column is as large as 0.20, this level of agreement strongly validates the EIT method. Values of $\bar{\varepsilon}_G$ were also determined from EIT and GDT by analytically averaging the profiles of Figure 14 over the column area. Figure 15 shows these cross-sectionally-averaged gas volume fractions as a function of superficial gas velocity U_G. Again, the GDT and EIT values are in very good agreement, differing by no more than 0.01 in $\bar{\varepsilon}_G$.

Because of the difference in collection times for the two methods (about 23 minutes for GDT but less than 20 seconds for EIT), it was decided to look for slow oscillations in the flows which might be averaged out by GDT but not by EIT. Separate flow measurements were taken under the same churn-turbulent flow conditions with an impedance-based bulk void fraction meter described in detail by Torczynski *et al.* (1997). The voltage across the bulk meter electrodes was recorded over a period of ten minutes with a digitizing oscilloscope, and Fourier spectra were computed from the data to determine the frequencies of gas volume fraction fluctuations. Signal spectra revealed no coherent periodic flow behavior over the range of zero to 12.5 Hz; this alleviated the concern that EIT measurements were capturing data over only a portion of slow flow cycles. This conclusion has also been substantiated using differential-pressure measurements to estimate gas volume fraction in the fully developed flow region.

Signal-to-noise ratios were also computed from bulk meter voltage signals taken at flow and no-flow conditions. Using a sum-of-squares method, the noise measured without gas flow was subtracted from the total noise to estimate variations in the signals due solely to variations in gas volume fraction. Average voltages $\overline{V}$ were correlated with cross-sectionally-averaged gas volume fractions $\overline{\varepsilon}_G$ determined from concurrent GDT scans, and temporal variations in $\overline{\varepsilon}_G$ at each flow condition were estimated from the voltage variations and the correlation of $\overline{\varepsilon}_G$ versus $\overline{V}$. Table 4 compares $\Delta\overline{\varepsilon}_G^{Bulk}$, the estimate of these temporal variations, with $\overline{\varepsilon}_G^{EIT} - \overline{\varepsilon}_G^{GDT}$, the difference between the average values measured by EIT and GDT. Since $\Delta\overline{\varepsilon}_G^{Bulk}$ and $\overline{\varepsilon}_G^{EIT} - \overline{\varepsilon}_G^{GDT}$ are comparable, the different methods of temporal averaging by EIT and GDT may account for some of the difference between the two measured values $\overline{\varepsilon}_G^{EIT}$ and $\overline{\varepsilon}_G^{GDT}$. However, since the difference $\overline{\varepsilon}_G^{EIT} - \overline{\varepsilon}_G^{GDT}$ is small compared to both $\overline{\varepsilon}_G^{EIT}$ and $\overline{\varepsilon}_G^{GDT}$, both methods of temporal averaging appear to be benign. Future investigations will examine the effects of temporal averaging by EIT and GDT more closely.

5. CONCLUSIONS

The Sandia EIT system and reconstruction algorithm have been validated for the measurement of solid volume fractions in solid-liquid flows and gas volume fractions and radial profiles in gas-liquid flows. EIT was used to measure solid volume fractions of up to 0.05, with excellent agreement between EIT results and the nominal values determined from the mass of solids in each flow. Gas-liquid bubble-column flows were measured with EIT and GDT; for cross-sectionally-averaged gas volume fractions up to 0.15, the average values and radial profiles from EIT and GDT agreed to within 0.01, despite large

radial variations across the column. The Maxwell-Hewitt relations used to convert conductivity information to insulating phase distributions were found to be accurate for cases where the assumptions inherent in their derivation were valid.

Future work will extend the use of EIT and GDT to three-phase flows in a slurry bubble column, so that the effect of the solid phase on hydrodynamic behavior may be examined. The study will employ a solid phase with conductive properties similar to air and a density similar to water, so that EIT will detect both the solid and gas phases but GDT will detect only the gas phase. The difference in the radial profiles from the two reconstruction methods will yield a radial solids distribution in the three-phase flow. This will represent another step toward the application of EIT to industrial multiphase flows.

Acknowledgments --- This work was performed at Sandia National Laboratories. Sandia is a multiprogram laboratory operated by Sandia Corporation, a Lockheed Martin Company, for the United States Department of Energy under Contract DE-AC04-94AL85000. A portion of this work was funded by the Federal Energy Technology Center under Field Work Proposal FEW 8616. The authors are grateful for technical interactions with Dr. Bernard A. Toseland of Air Products and Chemicals, Inc. The authors would also like to thank C. B. Lafferty and W. C. Ginn for their skilled technical assistance, D. R. Adkins for his early work with the GDT system, and A. T. Leger for her early work with the EIT system.

REFERENCES

Adkins, D. R., Shollenberger, K. A., O'Hern, T. J., and Torczynski, J. R. (1996) Pressure effects on bubble column flow characteristics. *ANS Proceedings of the 1996 National Heat Transfer Conference*, American Nuclear Society, LaGrange Park, IL, THD-Vol. **9**, 318-325.

Ceccio, S. L., and George, D. L. (1996) A review of electrical impedance techniques for the measurement of multiphase flows. *J. Fluids Eng.* **118**, 391-399.

Dickin, F. J., Williams, R. A., and Beck, M. S. (1993) Determination of composition and motion of multicomponent mixtures in process vessels using electrical impedance tomography — I. Principles and process engineering applications. *Chem. Eng. Sci.* **48**, 1883-1897.

Fluid Dynamics International. (1995) *FIDAP Users Manual*, Fluid Dynamics International, Evanston, IL.

George, D. L., Ceccio, S. L., Shollenberger, K. A., Torczynski, J. R., and O'Hern, T. J. (1998) Comparison of electrical-impedance tomography and gamma-densitometry tomography for the measurement of gas volume fraction profiles in a bubble column. *Proceedings of the 1998 ASME Fluids Engineering Division Summer Meeting*, FED-Vol. **245**, No. 98-5081.

Hewitt, G. F. (1978) *Measurement of Two-Phase Flow Parameters*, Academic Press, London.

Huang, S. M., Plaskowski, A. B., Xie, C. G., and Beck, M.S. (1989) Tomographic imaging of two-component flow using capacitance sensors. *J. Phys. E: Sci. Instr.* **22**, 173-177.

Jackson, N. B., Torczynski, J. R., Shollenberger, K. A., O'Hern, T. J., and Adkins, D. R. (1996) Hydrodynamic characterization of slurry bubble-column reactors for Fischer-Tropsch synthesis. *Proceedings of the Thirteenth Annual International Pittsburgh Coal Conference, Vol. 2: Coal-Energy and the Environment,* S.-H. Chiang, ed., University of Pittsburgh Center for Energy Research, Pittsburgh, PA, 1226-1231.

Jones, O. C., Lin, J.-T., and Ovacik, L. (1992) Investigation of electrical impedance imaging relative to two-phase, gas-liquid flows. *Chem. Eng. Comm.* **118**, 299-325.

Jones, O. C., Lin, J.-T., Ovacik, L., and Shu, H. (1993) Impedance imaging relative to gas-liquid systems. *Nucl. Eng. Design* **141**, 159-176.

Jones, O. C., Lin, J. T., Shu, H., Ovacik, L., and He, Y. (1994) Impedance imaging relative to binary mixtures. *Fifth International Symposium on Liquid-Solid Flows*, American Society of Mechanical Engineers, Lake Tahoe, Nevada.

Maxwell, J. C. (1881) *A Treatise on Electricity and Magnetism*, Clarendon Press, Oxford, England.

O'Hern, T. J., Torczynski, J. R., Ceccio, S. L., Tassin, A. L., Chahine, G. L., Duraiswami, R., and Sarkar, K. (1995) Development of an electrical-impedance tomography system for an air-water vertical bubble column. *ASME Forum on Measurement Techniques in Multiphase Flows*, T. J. O'Hern, A. Naqwi, C. Presser, and R. D. Skocypec, eds., American Society of Mechanical Engineers, New York, FED-Vol. **233**, 531-537.

Plaskowski, A., Beck, M. S., Thorn, R., and Dyakowski, T. (1995) *Imaging Industrial Flows: Applications of Electrical Process Tomography,* Institute of Physics Publishing, Bristol, England.

Reinecke, N., and Mewes, D. (1997) Multielectrode capacitance sensors for the visualization of transient two-phase flows. *Exp. Thermal Fluid Sci.* **15**, 253-266.

Shollenberger, K. A., Torczynski, J. R., Adkins, D. R., O'Hern, T. J., and Jackson, N. B. (1997a) Gamma-densitometry tomography of gas holdup spatial distribution in industrial-scale bubble columns. *Chem. Eng. Sci.* **52**, 2037-2048.

Shollenberger, K. A., Torczynski, J. R, O'Hern, T. J., Adkins, D. R., Ceccio, S. L., and George, D. L. (1997b) Comparison of gamma-densitometry tomography and electrical-impedance tomography for determining material distribution in liquid-solid flows. *Proceedings of the 1997 ASME Fluids Engineering Division Summer Meeting*, J. Katz and K. J. Farrell, eds., American Society of Mechanical Engineers, New York, Vol. FEDSM '97, No. 97-3690.

Thoraeus, R. (1965) Attenuation of gamma radiation from ^{60}Co, ^{137}Cs, ^{192}Ir, and ^{226}Ra in various materials used in radiology. *Acta Radiologica* **3**, 81-86.

Torczynski, J. R., O'Hern, T. J., Shollenberger, K. A., Ceccio, S. L., and Tassin, A. L. (1996a) Finite element method electrical-impedance tomography for phase distribution determination in multiphase flows: validation calculations and experiments. *ASME Cavitation and Multiphase Flow Forum,* J. Katz and K. J. Farrell, eds., American Society of Mechanical Engineers, New York, FED-Vol. **236**, 497-501.

Torczynski, J. R., Adkins, D. R., Shollenberger, K. A., and O'Hern, T. J. (1996b) Application of gamma-densitometry tomography to determine phase spatial variation in two-phase and three-phase bubbly flows. *ASME Cavitation and Multiphase Flow Forum,* J. Katz and K. J. Farrell, eds., American Society of Mechanical Engineers, New York, FED-Vol. **236**, 503-508.

Torczynski, J. R., O'Hern, T. J., Adkins, D. R., Jackson, N. B., and Shollenberger, K. A. (1997) *Advanced Tomographic Flow Diagnostics for Opaque Multiphase Fluids*, Report SAND97-1176, Sandia National Laboratories, Albuquerque, NM.

Vest, C. M. (1985) Tomography for properties of materials that bend rays: a tutorial. *Appl. Opt.* **24**, 4089-4094.

Webster, J. G., ed. (1990) *Electrical Impedance Tomography*, Adam Hilger, Bristol, England.

Yorkey, T. J., Webster, J. G., and Tompkins, W. J. (1987) Comparing reconstruction methods for electrical impedance tomography. *IEEE Trans. Biomedical Eng.* **11**, 843-852.

Table 1. Fundamental EIT voltage solutions for 16 strip electrodes in the transparent bubble column

Fundamental voltage	Computational value	Experimental value	Experimental value × 1.007
V_0 (reference)	0	0	0
V_1	0.002275	0.002295	0.002311
V_2	0.009430	0.009481	0.009546
V_3	0.02260	0.02252	0.02267
V_4	0.04432	0.04392	0.04422
V_5	0.08030	0.07963	0.08018
V_6	0.1454	0.1443	0.1453
V_7	0.2947	0.2930	0.2950
V_8 (current-bearing)	1.327	1.232	1.241

Table 2. Effect of FEMEIT mesh refinement on reconstruction accuracy. Analytical solution is $\gamma = 1$

Mesh	Number of nodes	Number of elements	Computed γ
A	25	32	1.0443
B	81	128	1.0122
C	169	288	1.0047
D	289	512	1.0023
E	441	800	1.0013

Table 3. Comparison of actual and reconstructed geometries of insulating inclusions in two-dimensional validation tests

Actual conditions			PC electrode section (slow mode)			IC electrode selection (fast mode)		
$d/2R$	z/R	$\bar{\varepsilon}$	$d/2R$	z/R	$\bar{\varepsilon}$	$d/2R$	z/R	$\bar{\varepsilon}$
0	-	0	0.062	0.000	0.004	0.059	0.000	0.004
0.266	0.596	0.071	0.271	0.597	0.074	0.271	0.597	0.074
0.300	0.000	0.090	0.309	0.020	0.095	0.308	0.020	0.095
0.534	0.189	0.285	0.530	0.184	0.281	0.530	0.184	0.280

Table 4. Comparison of differences between EIT and GDT with temporal fluctuations in gas volume fraction measured by the bulk void fraction meter

U_G (cm/s)	$\bar{\varepsilon}_G^{EIT}$	$\bar{\varepsilon}_G^{GDT}$	$\bar{\varepsilon}_G^{EIT} - \bar{\varepsilon}_G^{GDT}$	$\Delta\bar{\varepsilon}_G^{Bulk}$
1.5	0.044	0.038	0.006	0.015
2.9	0.076	0.077	-0.001	0.016
4.4	0.103	0.095	0.008	0.018
5.9	0.123	0.109	0.014	0.020
8.8	0.158	0.149	0.009	0.023

Figure 1.

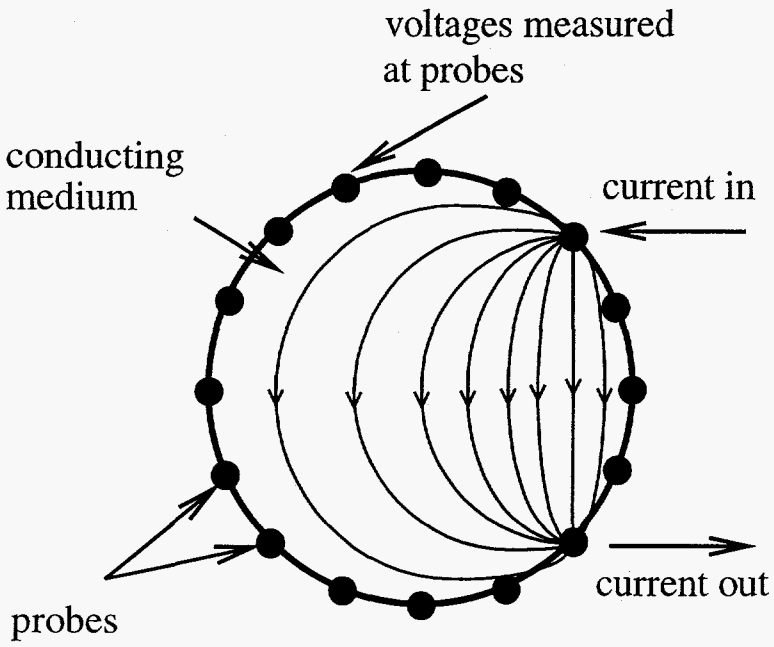

Figure 2.

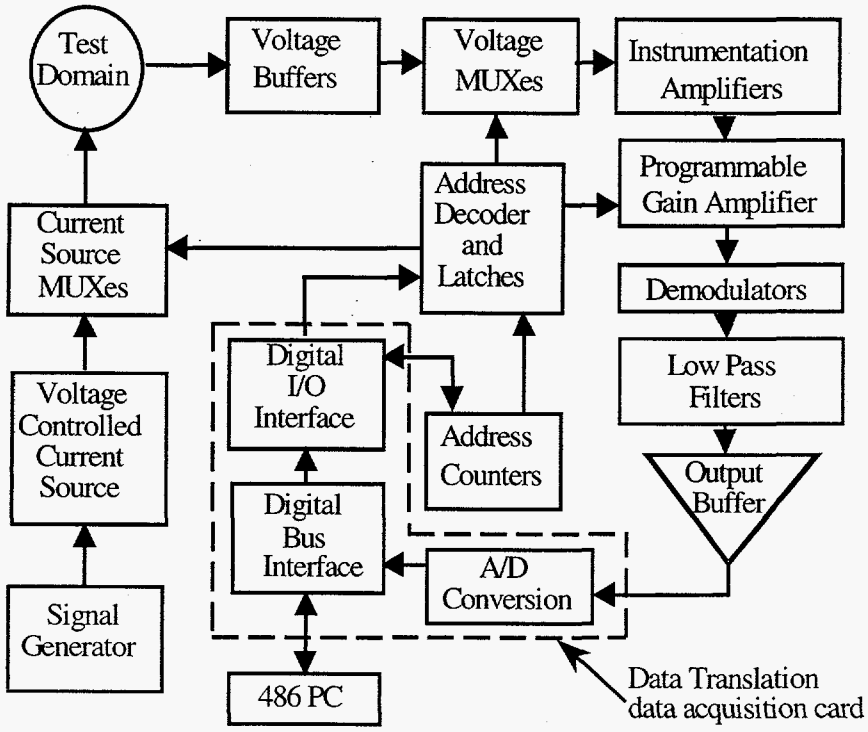

Figure 3.

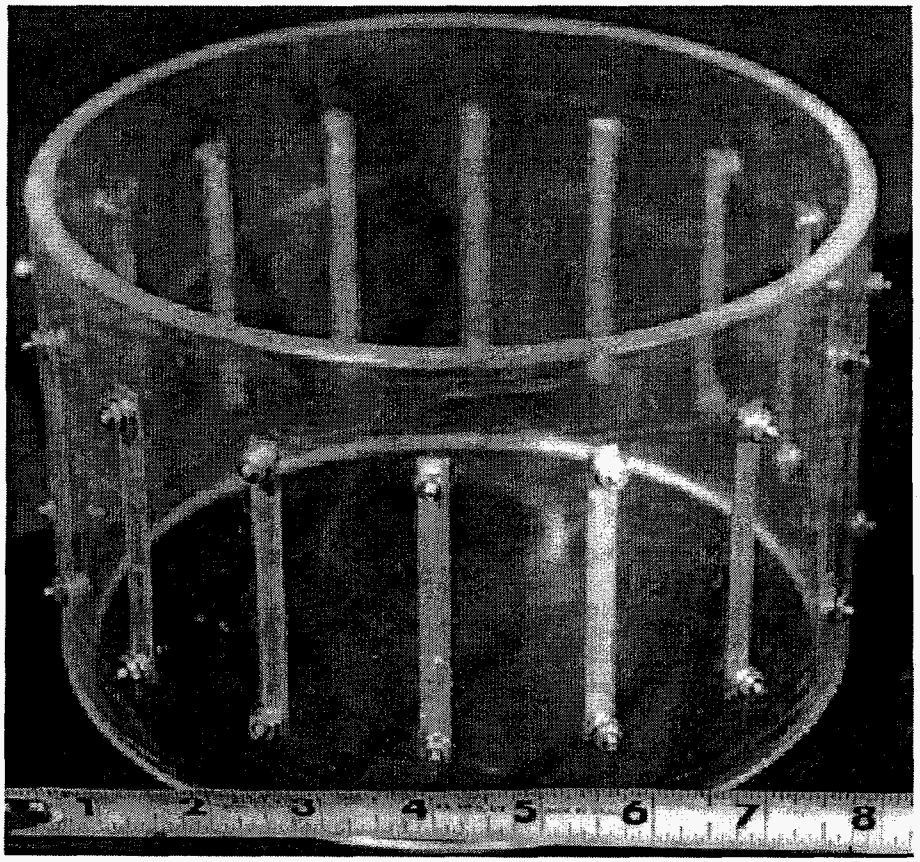

Figure 4.

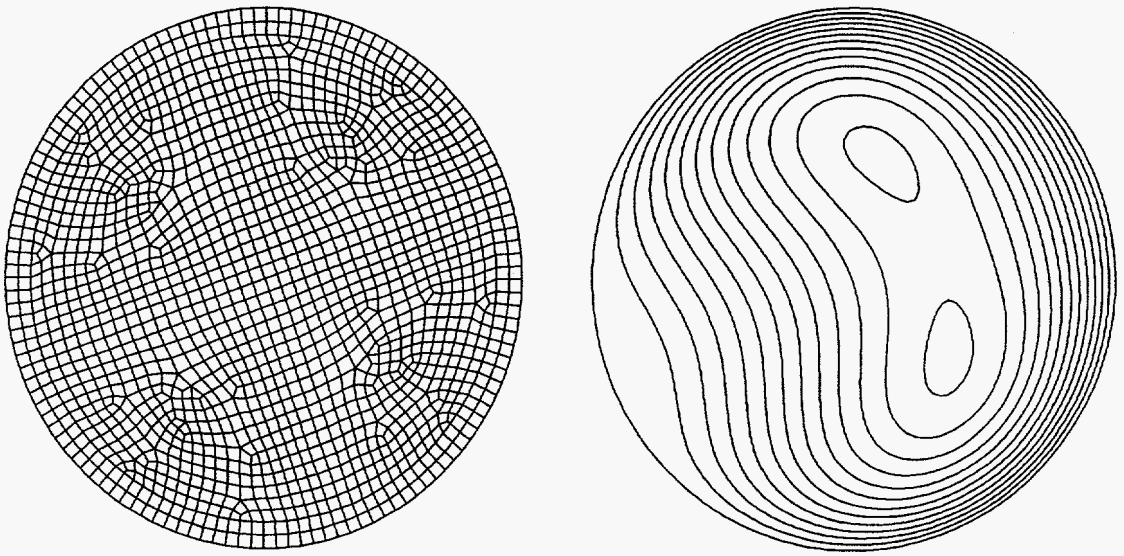

Figure 5.

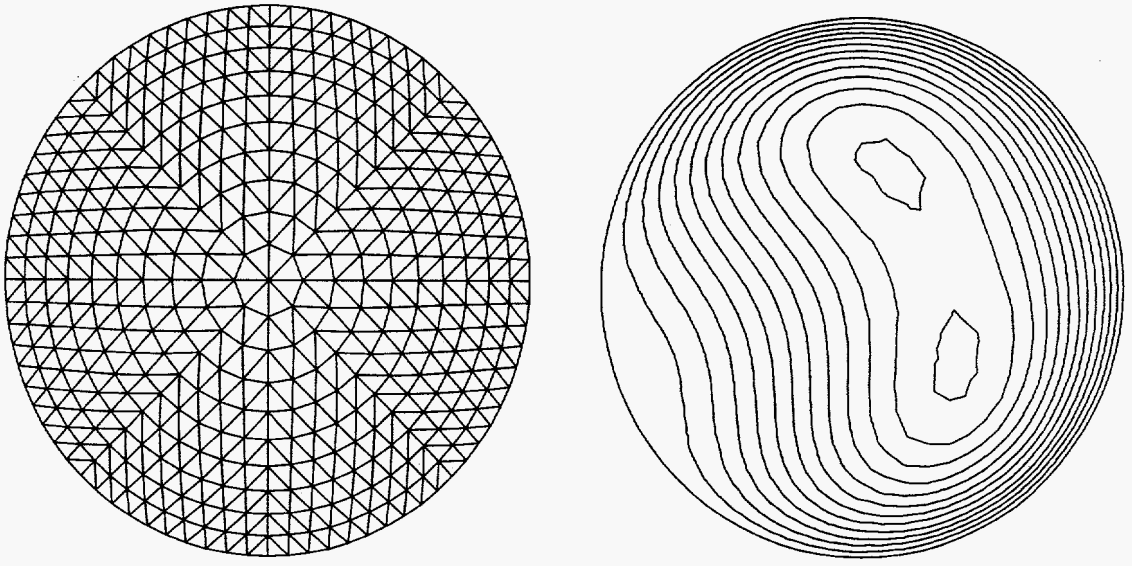

Figure 6(a) (above) and (b) (below).

Figure 7.

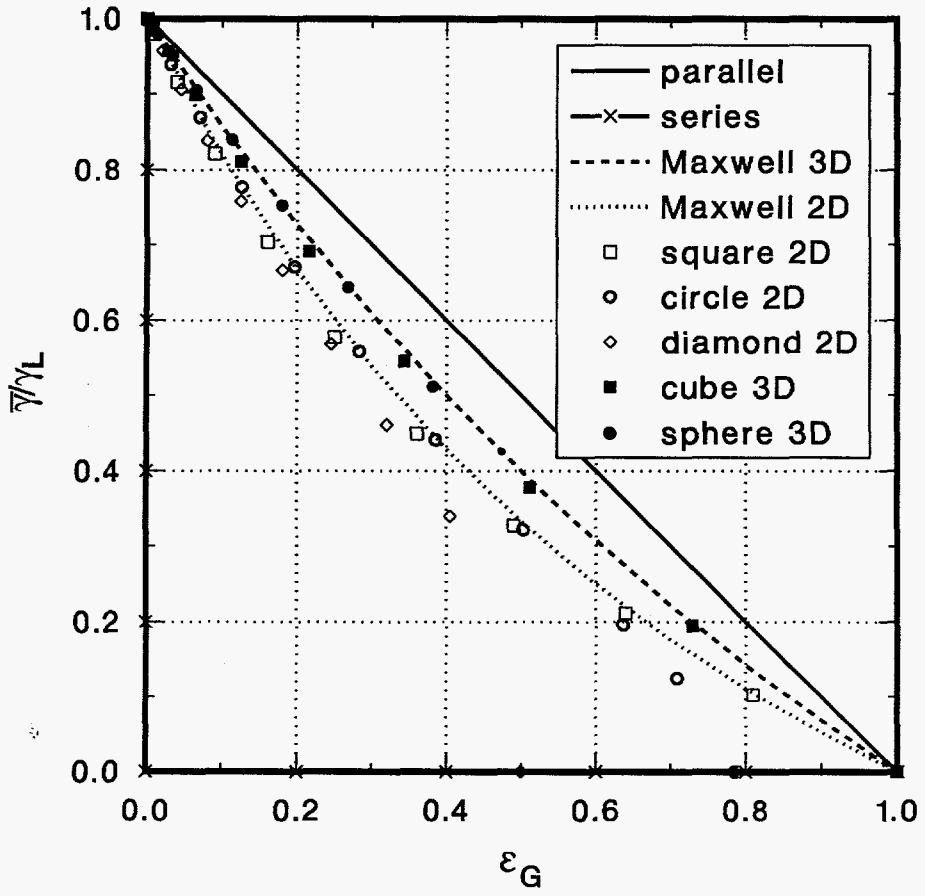
1.0
0.8
0.6
0.4
0.2
0.0
0.0
0.2
0.4
0.6
0.8
1.0
$\overline{\gamma}/\gamma_L$
ε_G
parallel
series
Maxwell 3D
Maxwell 2D
square 2D
circle 2D
diamond 2D
cube 3D
sphere 3D

Figure 8.

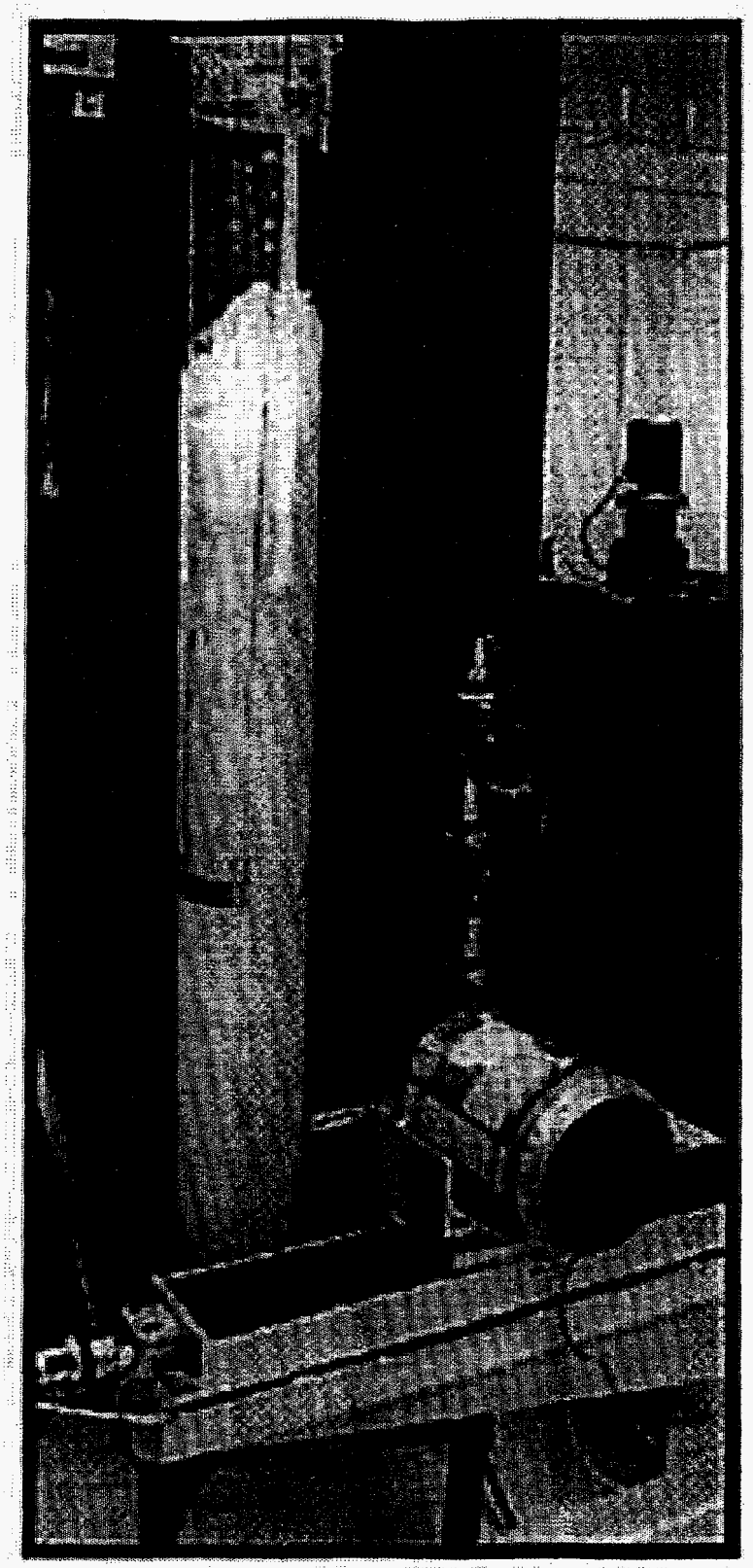

Figure 9.

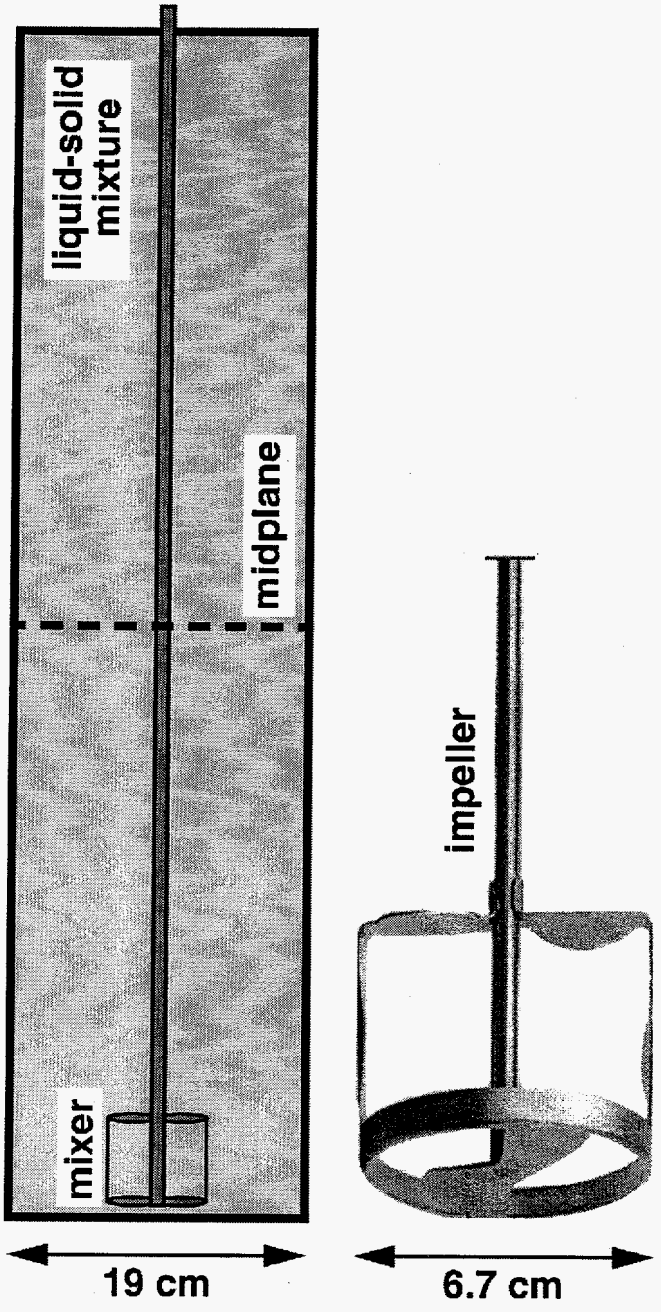

Figure 10.

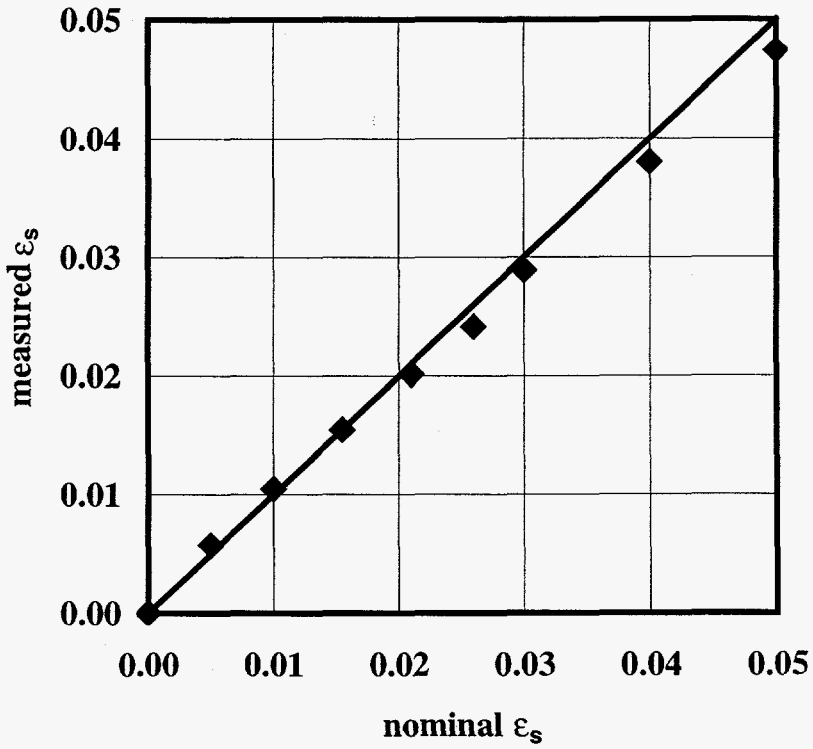
0.05
0.04
0.03
0.02
0.01
0.00
measured ε_s
0.00
0.01
0.02
0.03
0.04
0.05
nominal ε_s

Figure 11.

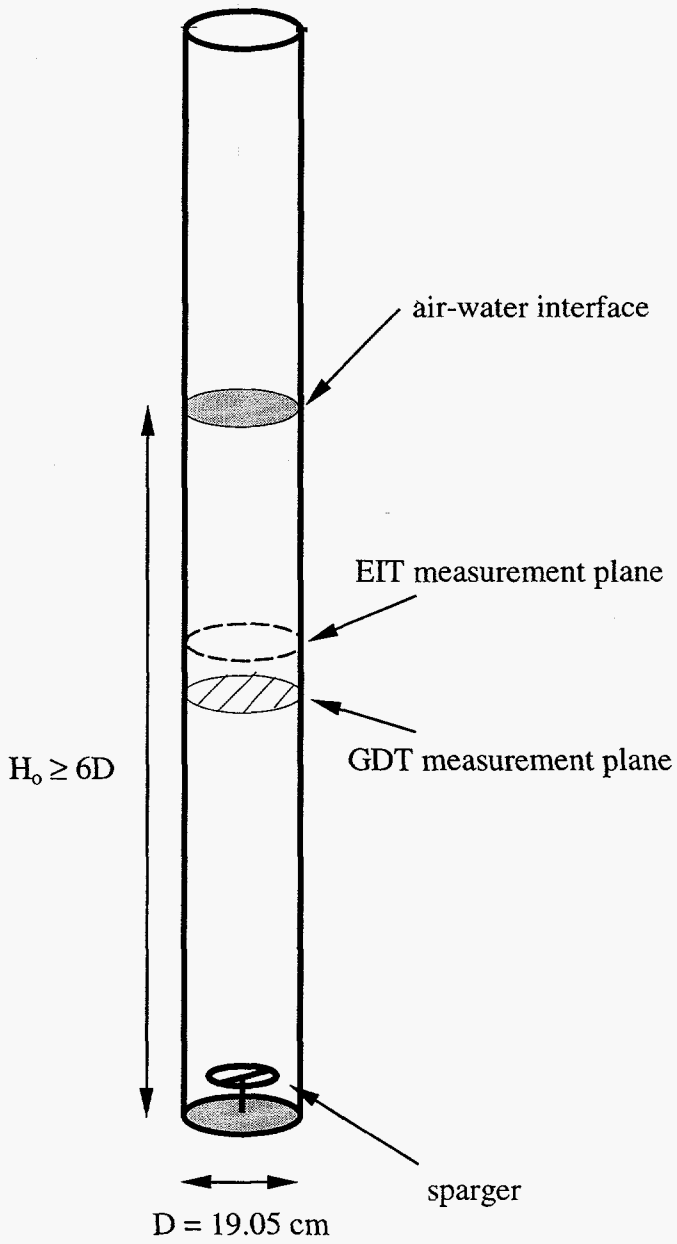
air-water interface
EIT measurement plane
GDT measurement plane
$H_o \geq 6D$
sparger
D = 19.05 cm

Figure 12.

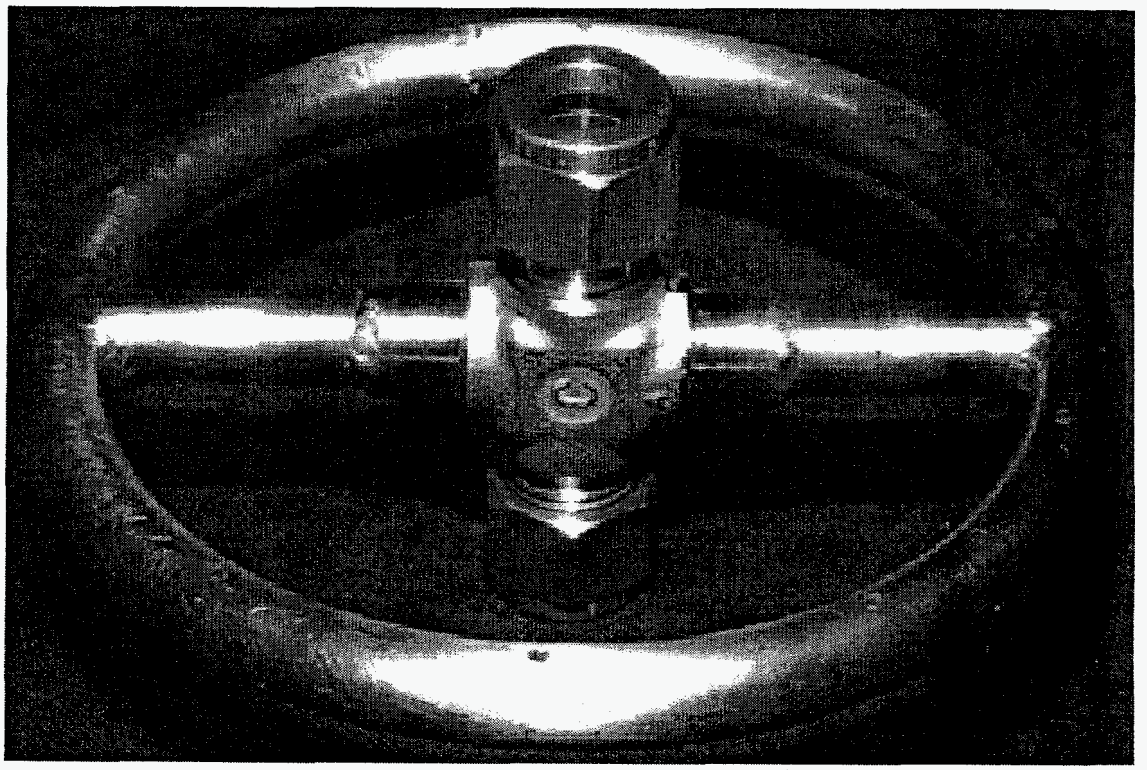

Figure 13(a).

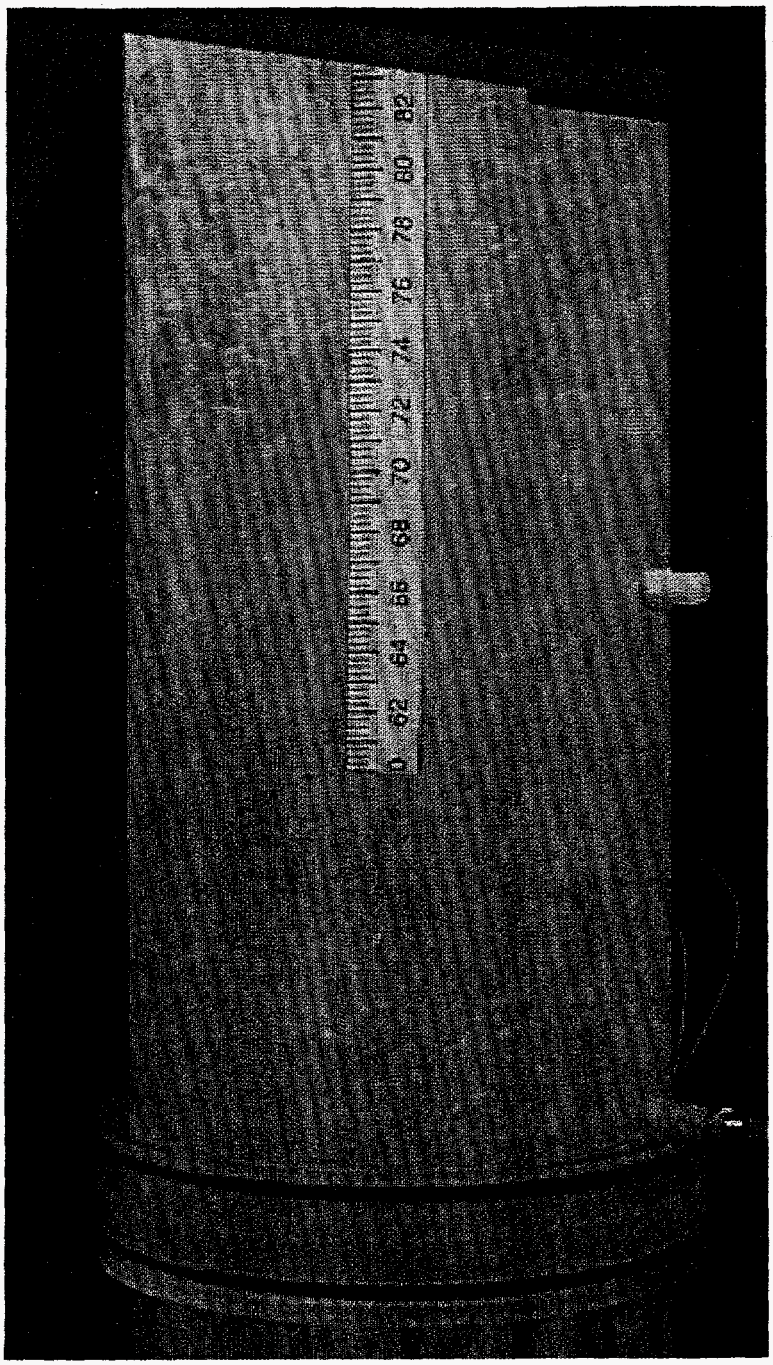

Figure 13(b).

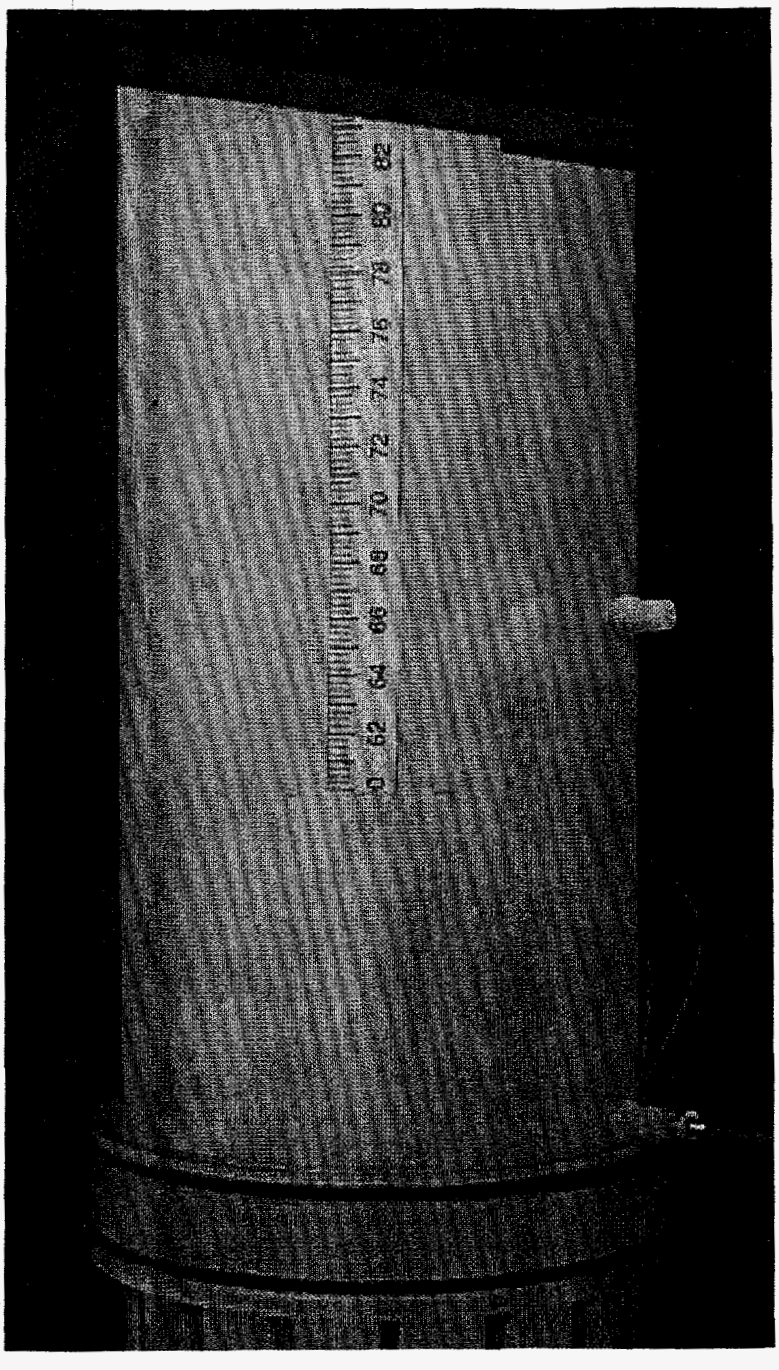

Figure 14(a) (above) and (b) (below).

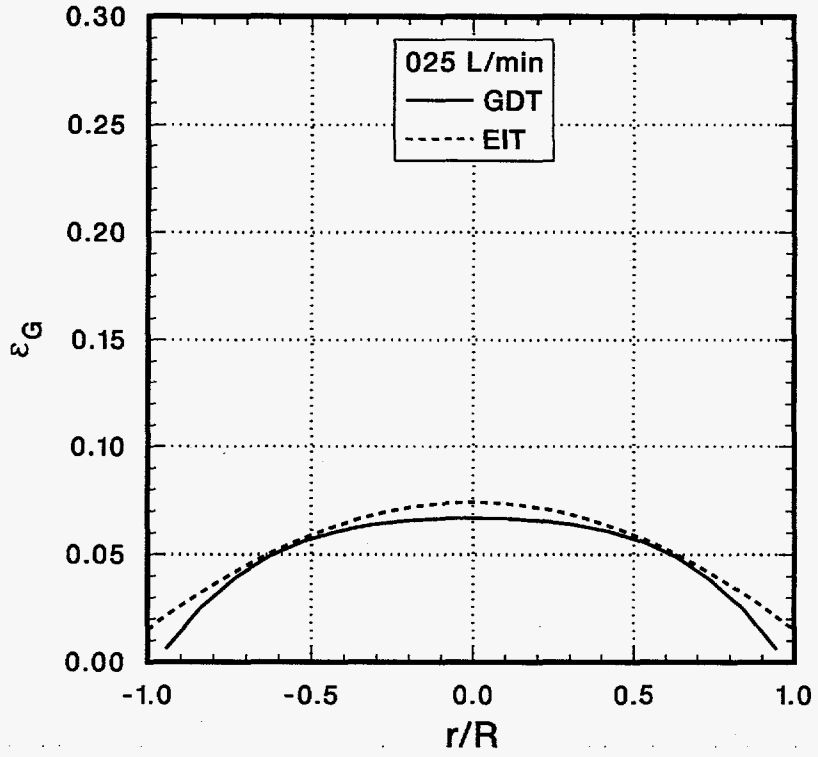

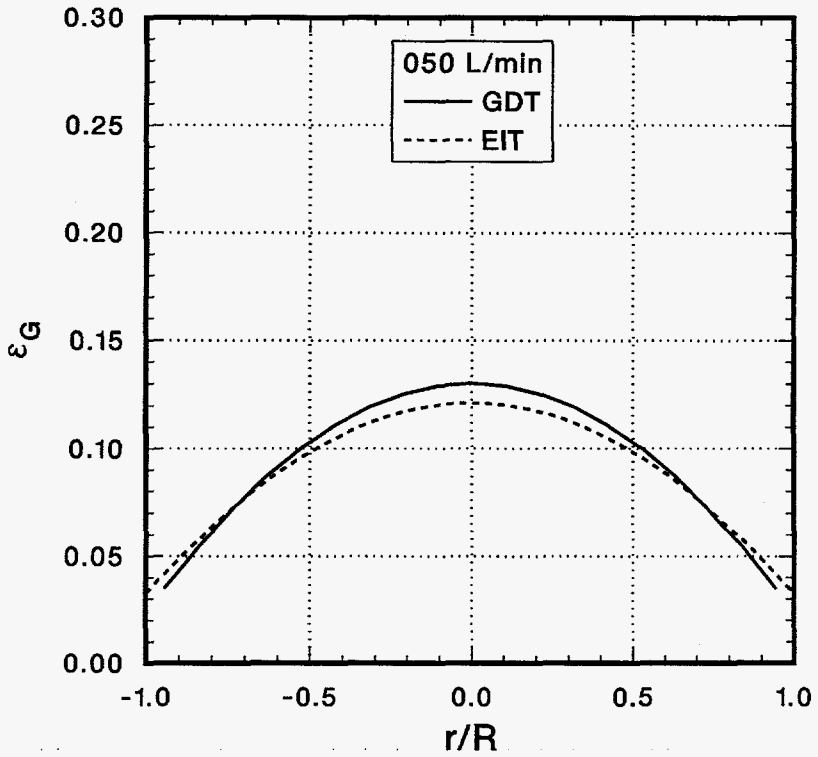

Figure 14(c) (above) and (d) (below).

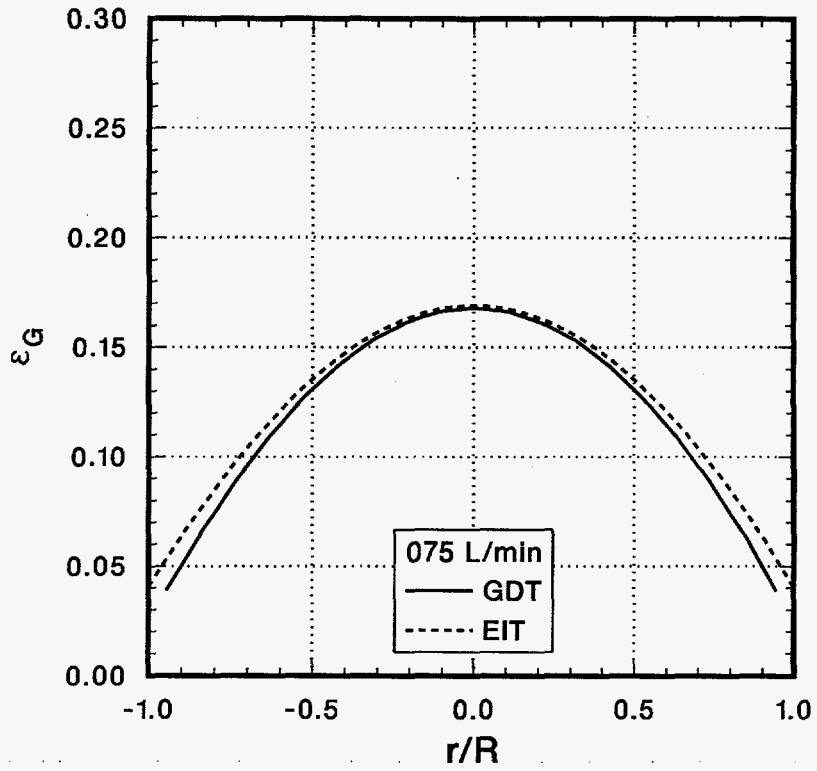

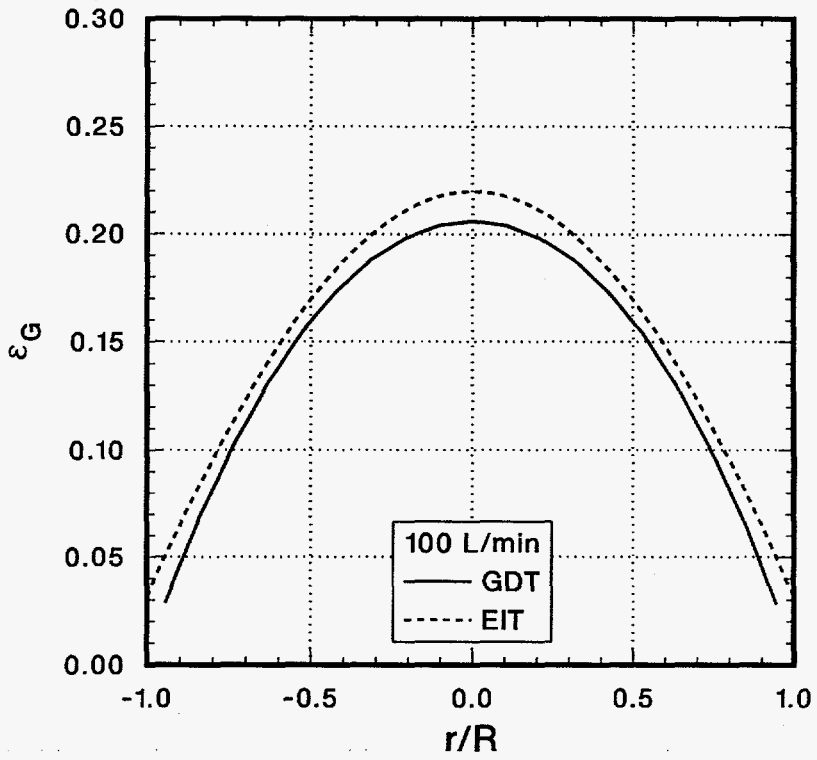

Figure 14(e).

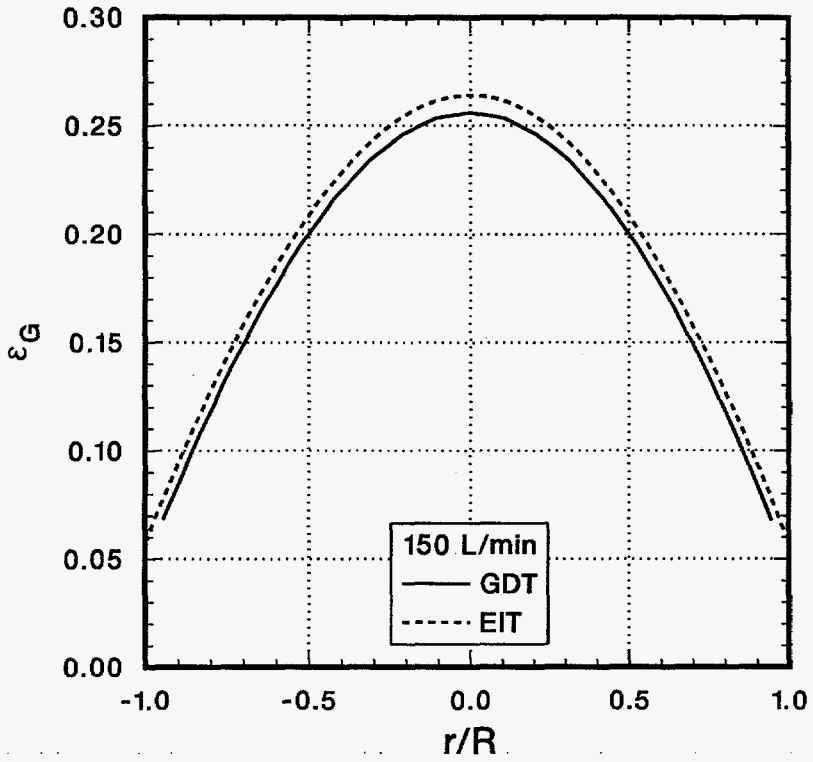

Figure 15.